PERIODICO di MINERALOGIA
established in 1930

DIPARTIMENTO
DI SCIENZE DELLA TERRA

SAPIENZA
UNIVERSITÀ DI ROMA

An International Journal of
Mineralogy, Crystallography, Geochemistry,
Ore Deposits, Petrology, Volcanology
and applied topics on Environment, Archaeometry and Cultural Heritage

First occurrence, crystal-chemistry and structure of erionite, a carcinogenic fibrous zeolite, from the volcanic rocks of Latium (Italy)

Michele Mattioli [1,*], Matteo Giordani [1], Paolo Ballirano [2], Emma Salvioli-Mariani [3], Simone Bernardini [4], Giancarlo Della Ventura [4,5]

[1] Department of Pure and Applied Sciences, University of Urbino Carlo Bo, via Cà Le Suore 2/4, 61029 Urbino (PU), Italy
[2] Department of Earth Sciences, Sapienza University of Rome, Piazzale Aldo Moro 5, 00185 Roma, Italy
[3] Department of Chemistry, Life Sciences and Environmental Sustainability, University of Parma, Parco Area Delle Scienze 157/A, 43124, Parma, Italy
[4] Department of Geological Sciences, University of Roma Tre, Largo San Leonardo Murialdo 1, 00146 Roma, Italy
[5] INFN-Istituto Nazionale Di Fisica Nucleare, Via Enrico Fermi 54, 00044 Frascati (Roma), Italy

ARTICLE INFO

Submitted: May 2023
Accepted: June 2023
Available on line: July 2023

* Corresponding author:
michele.mattioli@uniurb.it

Doi: 10.13133/2239-1002/18084

How to cite this article:
Mattioli M. et al. (2023)
Period. Mineral. 92, 159-178

ABSTRACT

This work relates to the occurrence and crystal-chemical characterization of fibrous erionite, a carcinogenic zeolite, discovered for the first time in the volcanic rocks of Latium, Italy. The erionite samples were investigated using SEM, TGA, PXRD, FTIR and Raman spectroscopies. Cell parameters, fractional coordinates and site scattering were refined using the Rietveld method. Two different types of erionite were found, having different crystal morphologies, chemical composition, and structure. The first type is an extremely fibrous erionite-K, with Si/(Si+Al) ratio of 0.77, cell parameters a=13.255 Å, c=15.053 Å and cell volume V=2290.49 Å^3. The second type is acicular to highly fibrous erionite-Na, with a lower Si/(Si+Al) ratio (0.72-0.73) and larger cell parameters (a=13.291 Å, c=15.146 Å, cell volume V=2317.35 Å^3). Both erionite types occur as fibers of inhalable size. The structure of both samples, refined by the Rietveld method on powder X-ray diffraction data, collected in transmission mode on capillaries, is consistent with that of samples with similar extra-framework cations content. Raman and FTIR data are presented and discussed.
The described finding of potentially carcinogenic erionite in the volcanic rocks of Latium that are typically rich in zeolites of various nature, both as cavity filling and devitrification products of glass, suggests that this hazardous mineral might be more common than previously believed in the area and points to the need for detailed and more systematic studies.

Keywords: erionite; fibrous zeolites; toxicity; Latium; powder X-ray diffraction, SEM-EDS, FTIR and Raman spectroscopies.

INTRODUCTION

Fibrous minerals are well-known to have adverse effects on human health, a piece of evidence that stems from decades of studies of toxicity, carcinogenicity and epidemiological data on asbestos minerals (Gualtieri, 2017, 2023 and reference therein). Asbestos is a term presently related to six minerals: one-layer silicate, i.e., chrysotile (serpentine group), and five double-chain

silicates (amphibole group), i.e., actinolite asbestos, amosite, anthophyllite asbestos, crocidolite and tremolite asbestos. These fibers are classified as Group 1, i.e., carcinogenic to humans, together with fibrous erionite that, instead, belongs to the zeolite group (IARC, 2012). Although erionite is currently the only regulated fibrous zeolite, many recent studies have shown that other zeolite species could have negative effects on human health, such as ferrierite (Gualtieri et al., 2018; Zoboli et al., 2019; Mattioli et al., 2022), offretite (Mattioli et al., 2018; Giordani et al., 2019), mordenite (Di Giuseppe, 2020; Giordani et al., 2022a), thomsonite and mesolite (Giordani et al., 2022b), scolecite (Mattioli et al., 2016). Evidences of potential toxicity have been also recently obtained for other elongated mineral particles (EMPs): fluoro-edenite (Comba et al., 2003; Gianfagna et al., 2003; Cardile et al., 2004), winchite (Erskine and Bailey, 2018), richterite (Sullivan, 2007; Pacella and Ballirano, 2016; Rogers, 2018;), fibrous glaucophane (Erskine and Bailey, 2018; Di Giuseppe et al., 2019; Gualtieri et al., 2021), fibrous antigorite (Cardile et al., 2007; Petriglieri et al., 2021), balangeroite (Groppo et al., 2005; Turci et al., 2009) and also epsomite (Giordani et al., 2022c), talc and the clay minerals sepiolite and palygorskite (García-Romero and Suàrez, 2013; Larson et al., 2016). To date, erionite shows the highest toxic and carcinogenic potential, even higher than asbestos (Coffin et al., 1992; Carbone et al., 2011).

Erionite is potentially present in several areas worldwide where rock deposits possibly containing this zeolite crop out. Great attention has been initially paid by the scientific community and authorities in Turkey, where the relation erionite-lung cancer was first demonstrated (Carbone et al., 2011, 2019), then in USA (Carbone et al., 2011), Mexico (Saini-Eidukat and Triplet, 2014; Ortega-Guerrero et al., 2014), Italy (Giordani et al., 2016, 2017), New Zealand (Patel et al., 2021) and Iran (Ilgren et al., 2015). Many aspects of erionite and its capability to generate lung disease are still unknown, notwithstanding the number of performed studies on specific particular physical-chemical properties, surface reactivity, interacting capability and toxicity (e.g., Pollastri et al., 2014; Mattioli et al., 2016b; Cangiotti et al., 2018; Giordani et al., 2022b).

Erionite occurs mainly as a diagenetic alteration product of sediments, in vesicles and cavities of altered basalts (Mattioli et al., 2016a), or as a hydrothermal alteration product (Gottardi and Galli, 1985). Six characteristic geological settings were recognized for erionite formation by Patel et al. (2023): hydrothermal alteration of silica-rich volcanic deposits, diagenesis within lacustrine paleoenvironments, diagenesis within mafic rocks, hydrothermal alteration of intermediate to mafic rocks, rarely diagenetic product in a marine environment, and hydrothermal alteration via meteorite impact metamorphism.

Erionite occurs with various habits, from prismatic, elongated crystals to extremely fibrous and asbestiform (Mattioli et al., 2016b; Giordani et al., 2016; 2017). It belongs to the ABC-6 family, with a space group $P6_3/mmc$, unit-cell parameters a=13.19-13.34 Å, c=15.04-15.22 Å; the idealized chemical formula is $K_2(NaCa_{0.5})_8[Al_{10}Si_{26}O_{72}]\cdot 28H_2O$ (Gottardi and Galli, 1985; Passaglia et al., 1998; Armbruster and Gunter, 2001). Three species were recognized based on the most abundant extra-framework (EF) cation: erionite-K, erionite-Ca, and erionite-Na (Coombs et al., 1997). Structurally, the unit cell can be described based on two erionite (23-hedron) cages, two cancrinite (ε) cages, and two double-6 rings (D6R). Erionite and cancrinite cages host the EF cations (erionite: Ca1, Ca2, Ca3, K2; cancrinite: K1), while H_2O sites (OW7, OW8, OW9, OW10, OW11, OW12) are located around the axis of the cage coordinating the cations (Ballirano et al., 2017).

Iron has been suspected to play an essential role in the toxicity of erionite. Detailed studies show that Fe may be surface-deposited (as nanoparticles or thin layers containing Fe) or ion-exchanged (including Fe released after protein injury inside the human body), participating in Fenton chemistry (Eborn and Aust, 1995; Carr and Frey, 1999; Fach et al., 2003; Ballirano et al., 2015; Matassa et al., 2015; Gualtieri et al., 2016; Pacella et al., 2017 a,b; Gualtieri, 2018, 2021; Pacella et al., 2021).

Environmental and occupational exposures to erionite are crucial aspects that need to be assessed in Italy. Erionite was reported in Sardinia and Veneto regions (Passaglia and Galli, 1974; Pongiluppi et al., 1974; Giovagnoli and Boscardin, 1979; Passaglia and Tagliavini, 1995; Giordani et al., 2016, 2017), but a complete systematic investigation of its distribution is still missing. Giordani et al. (2017) suggest that this hazardous mineral may be more widespread than currently presumed, especially in suitable rock formations. However, erionite in volcanic rocks is often difficult to recognize and requires detailed fieldwork and several sampling phases. Moreover, the accurate characterization of erionite fibers needs a combination of several analytical techniques, most notably optical microscopy, scanning electron microscopy (SEM), powder X-ray diffraction (PXRD), and vibrational spectroscopy (Fourier Transform Infra-Red, FTIR, and Raman).

In this work, conducted within the project PRIN 2017 Fibres (Gualtieri et al., 2023, this volume), we present the first occurrence of fibrous erionite from the volcanic rocks of Latium, Central Italy. Detailed morphological, mineralogical, chemical and structural characterizations were performed using a multi-methodological approach, aiming to improve knowledge of this potentially hazardous zeolite.

GEOLOGICAL BACKGROUND

The erionite samples investigated in this study originate from the Vico Volcano, a stratovolcano cut by a summit caldera (Figure 1). The Vico Volcano and other volcanic districts (Vulsini, Sabatini, and Colli Albani) are part of the Roman Magmatic Province, which erupted about 900 km^3 of pyroclastic flow deposits and minor lavas between 800 and 20 ka (Peccerillo, 2005 and references therein). Rocks range from potassic (K-trachybasalt to trachyte) to ultrapotassic (leucite tephrite and leucitite to leucite phonolite) in composition (e.g., Perini et al., 2004; Conticelli et al., 2013).

The eruptive products of Vico (ca. 420-95 ka) are interfingered with the deposits of Vulsini and Sabatini and overlie the Monte Cimino dome complex (1.3-0.9 Ma). The Vico eruptive history can be summarized into 4 main periods (Nappi et al., 2016).

The first period comprises intermittent effusive and explosive phases aged between 420 and 400 ka. The pyroclastic products of the explosive phases can be referred

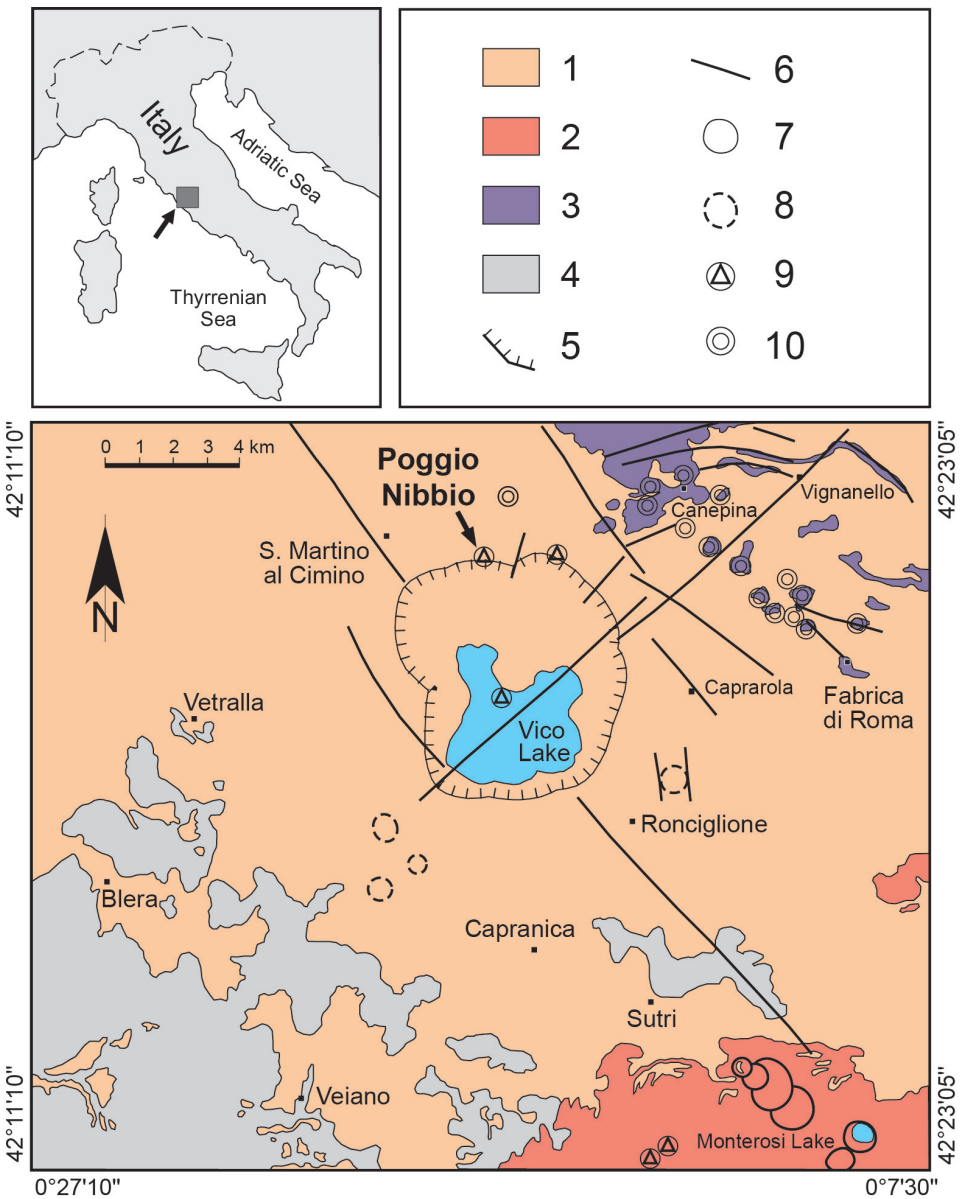

Figure 1. Geological sketch map of the Vico Volcano area (modified from Nappi et al., 2016), with the indication of the sampling site (Poggio Nibbio peri-caldera monogenic center). 1 = Vico volcanic rocks; 2 = Sabatini volcanic rocks; 3 = Cimini volcanic rocks; 5 = caldera rim; 6 main faults; 7 = crater; 8 = buried crater; 9 = monogenic center; 10 = lava dome.

to as a series of Plinian eruptions and are distributed NW, N and NE of the current apparatus. After a quiescence phase (~100 ka), an impressive effusive activity (second period, 305-258 ka) causes a continuous stacking of lava flows and originated the main stratovolcano. During the third period, a pivotal caldera-forming phase (ca. 250-144 ka) resulted from four significant explosive eruptions (ignimbrites A, B, C, D; Locardi, 1965). After the emission of the final ignimbrites, a lake basin is established inside the caldera. This situation determines a substantial variation of the type of activity, which evolved to hydromagmatic (fourth period, 138-95 ka). This final phase ends with an intense Strombolian and effusive activity located in the NE sector of the caldera, leading to the construction of the Monte Venere cone and peri- and intra-caldera monogenic centers (Figure 1).

Most of the pyroclastic deposits of the Vico Volcano are massive and consist of vitreous vesiculated juvenile scoriae, enclosed in an ashy matrix often lithified after zeolitization processes. The main minerals are chabazite and phillipsite, and the zeolitic content is locally variable, reaching 68% wt (Novembre et al., 2021). Zeolites usually grow by replacing amorphous fractions and pre-existing phases inside the matrix and scoriae. More rarely, lava flows and pyroclastic scoriae deposits show vesicles filled with secondary minerals, which are dominated by zeolites of hydrothermal origin.

EXPERIMENTAL

Materials

Two erionite samples (VV67a and VV67b) were investigated in this study. They are representative of the two different types of erionite found in several volcanic fragments sampled in a long-time idle pyroclastic quarry (42°21'45.9"N 12°09'51.3"E). These zeolites occur within the pyroclastic scoriae and lava fragments erupted during the final phase of the Vico Volcano, cropping out in the Poggio Nibbio sector (Figure 1). The host scoriae and lavas are poorly to highly vesiculated and vesicles are often filled with secondary minerals, including erionite (Figure 2).

Scanning Electron Microscopy (SEM-EDS)

Morphological observations were attained with a Quanta FEI 200 environmental scanning electron microscope (ESEM) equipped with an energy-dispersive spectrometer (EDS) for semi-quantitative chemical analyses at the University of Urbino Carlo Bo. Operating conditions were 30 kV accelerating voltage, 10 mm working distance, 0˚ tilt angle, and variable beam diameter. The ESEM was utilized in low vacuum mode, with a specimen chamber pressure set from 0.80 to 0.90 mbar.

Microchemical data were acquired by a JEOL 6400 SEM equipped with an Oxford Linkisis EDS system at the University of Parma. Operating conditions were 15 kV accelerating voltage, 1.2 nA beam current, 1 µm beam diameter, 10 mm working distance, 0° tilt angle and 60 s counting time. As suggested in previous studies (Sweatman and Long, 1969; Goldstein et al., 1992; Reed, 1993), Na and K were measured first by using a low counting time (from 100 s down to 50 s) and a raster scan mode, to reduce the temperature increase and minimize the alkali metal migration. Natural and synthetic standards were used for calibration.

The reliability of the chemical analysis was evaluated by using the charge balance error formula (E%: Passaglia, 1970; Passaglia et al., 1998), the Mg-content (Dogan and Dogan, 2008; Dogan et al., 2008) and K-content tests

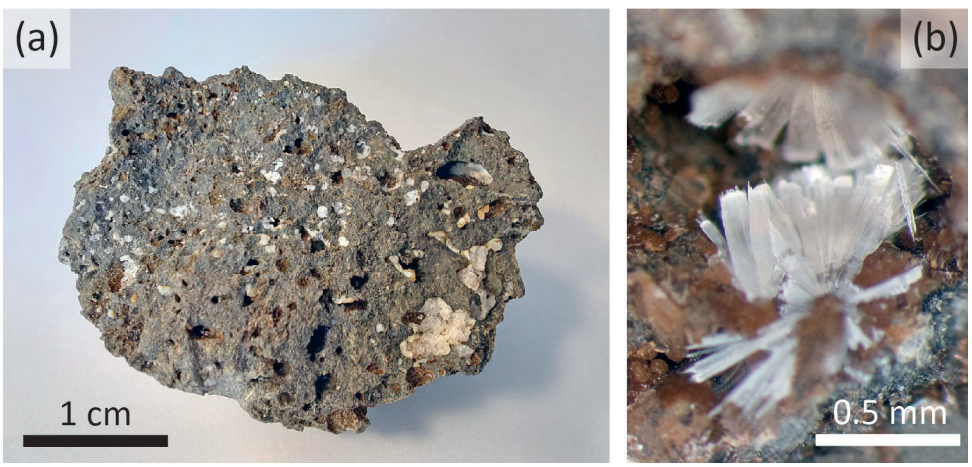

Figure 2. a) Vesiculated lava fragment from Poggio Nibbio monogenic center, with vesicles filled by secondary minerals, mainly represented by zeolites. b) Detail of a vesicle filled by fibrous erionite, corresponding to the VV67b-type.

(Cametti et al., 2013). In the case of zeolites, chemical analyses are considered reliable if the balance error (E%) is within ±10%.

Thermogravimetric analysis (TGA)

Thermogravimetric analysis (TGA) was performed on the VV67a sample using a TGA 400 (Perkin Elmer, Waltham, MA, USA) with a heating ramp of 10.0 °C/min under N_2 flow, in the temperature range 30-800 °C.

Powder X-ray Diffraction (PXRD)

The two samples were ground in an agate mortar and pestle and powders were loaded into a 0.6 mm (VV67a) and a 0.3 mm diameter (VV67b) sealed borosilicate capillary. The difference in diameter between the capillaries was due to the amount of powder available, which is very scarce in the case of VV67b. The capillaries were fixed to standard goniometer heads and aligned. Diffraction data were collected at Sapienza University of Rome using a Bruker AXS D8 Advance equipped with focusing Göbel mirrors along the incident beam and a position sensitive detector (PSD) VÅntec-1 set to an opening angle of 6° 2θ. The instrument operates in θ/θ transmission mode. Data were measured in the 5-145° 2θ angular range, 0.021798° 2θ step size, 40s counting time, using Cu Kα radiation. A preliminary check of the purity of the separated materials was performed using Bruker AXS DIFFRAC.EVA V5.1 software and PDF-2 release 2021 (ICDD, 2021) that pointed out the occurrence of minor plagioclase, calcite, quartz, 1:1 and/or 2:1 layer silicates (VV67a) and traces of calcite (VV67b) admixed to erionite. Structure analysis was performed by the mixed Pawley/Rietveld method described by Pacella et al. (2017a), using Topas V6 software (Bruker AXS, 2016). The software implements the Fundamental Parameters Approach (FPA: Cheary and Coelho, 1992) for describing the peak shape. Used starting structural data are listed in Table 1. Only the peak shape was refined for the minor phases. Absorption was corrected using the equation of Sabine et al. (1998) for a cylindrical sample. The correlation between displacement parameters and absorption was handled using the procedure described by Ballirano and Maras (2006). Spherical harmonics were applied to correct for minor preferred orientation effects, choosing the number of appropriate terms (8^{th}-order, six refinable parameters) according to Ballirano (2003). Refined structural parameters of erionite included fractional coordinates and site occupancy fraction (sof) of EF cations and H_2O sites. Isotropic displacement parameters were refined and constrained as follow: $B_{T1}=B_{T2}$; $B_{O1}=B_{O2}=B_{O3}=B_{O4}=B_{O5}=B_{O6}$; $B_{K1}=B_{K2}$; $B_{Ca1}=B_{Ca2}=B_{Ca3}=B_{Ow8}=B_{Ow9}=B_{Ow10}=B_{Ow11}=B_{Ow12}=2*B_{Ow7}$ to minimize correlations. To simplify the refinement process, following the same approach described in Quiroz et al. (2020), the minor contribution of layer silicates to the pattern of sample VV67a was approximated by single peaks at 2θ values (ca. 19.9°, 26.9°, 34.8°, 55.7°, 61.6°, 67.8°2θ) consistent with a hexagonal *a*=5.16 Å *c*=14.83 Å lattice. Therefore, quantification of layer silicates was not performed, but a rough estimate, based on relative peaks intensity, suggests a content well below 5 wt%.

Table 1. Reference data of the starting structural parameters used for fitting the contribution of minor phases occurring in a mixture with erionite in samples VV67a and VV67b.

Mineral species	Reference
Erionite	Cametti et al. (2013)
Plagioclase (anorthite)	Angel et al. (1990)
Calcite	Ballirano (2011)
Quartz	Le Page and Donnay (1976)

Vibrational (FTIR and Raman) spectroscopies

FTIR spectra were collected in the entire 7000-600 cm^{-1} range at INFN, Laboratori Nazionali di Frascati (Rome) using a Bruker Hyperion 3000 microscope attached to a Vertex V66 optical bench and equipped with a KBr beamsplitter and a MCT N2-cooled detector. The nominal resolution was set at 4 cm^{-1} averaging 128 scans on both peak and background. A beam size of 50 μm was used.

Raman measurements were performed at the Raman Spectra Lab, Department of Science, Roma Tre University, at room temperature using an inVia Renishaw spectrometer equipped with a diode laser (532 nm, output power 50 mW), an edge filter, 1800 lines per mm diffraction grating and a Peltier cooled 1024×256 pixel CCD detector. Samples were mounted on the manual stage of a Leica DM2700 M confocal microscope. In order to avoid sample degradation, neutral filters have been used to reduce the laser power to 5 mW. Spectral acquisitions (three accumulations, 30 s each) have been performed with a 50× objective. The Raman spectrometer was calibrated before the measurements using a Si wafer. The peak positions are estimated to be accurate to at least ±2 cm^{-1}.

RESULTS AND DISCUSSION

Scanning Electron Microscopy (SEM-EDS)

The two investigated erionite samples show different morphologic types whose main features are illustrated in the SEM images in Figure 3.

Sample VV67a is characterized by erionite with an

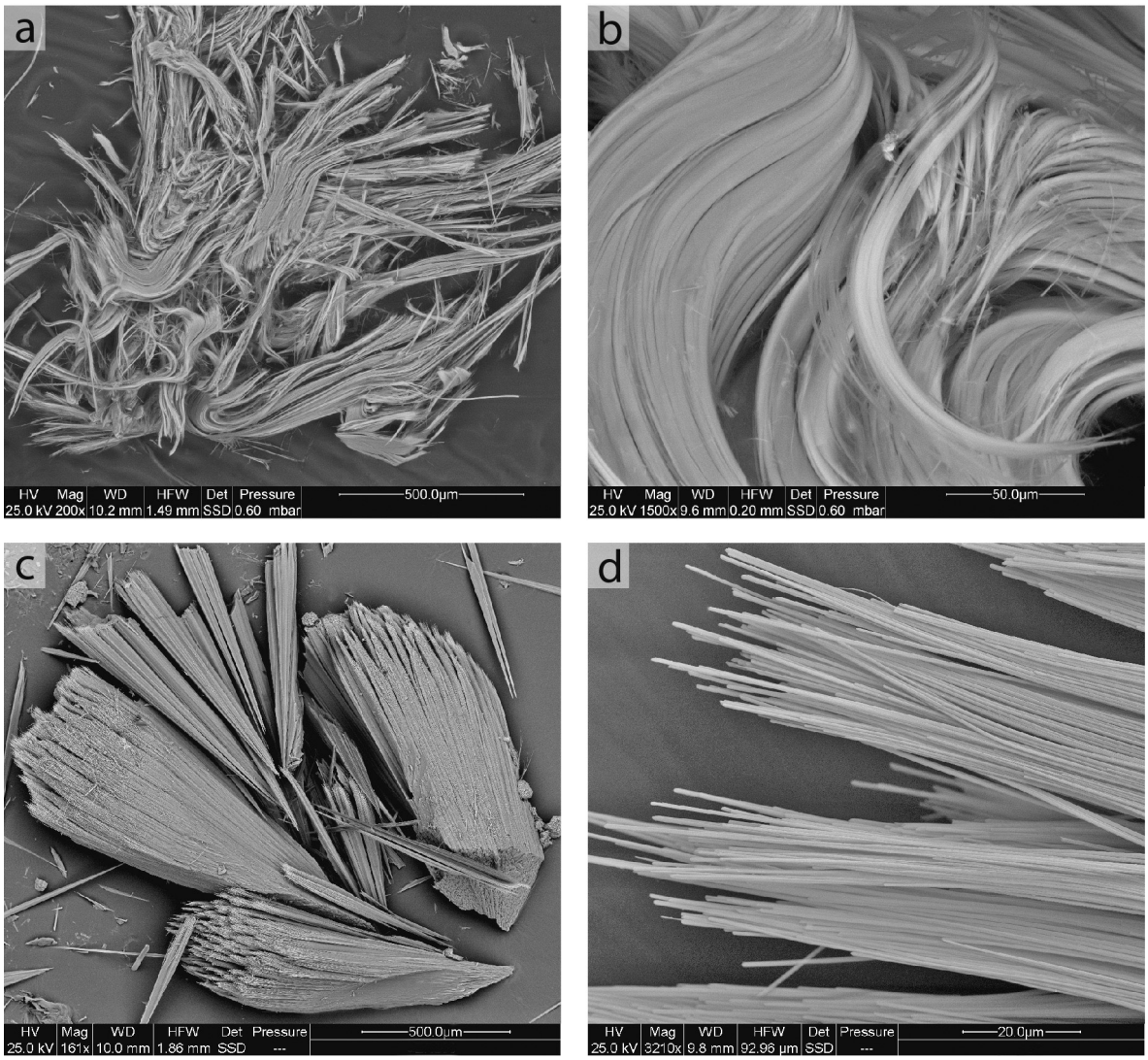

Figure 3. SEM images of the two different morphologic type of erionite investigated in this work: a) and b) erionite with an extremely fibrous habit and hair-like appearance (VV67a); c) and d) erionite with acicular to highly fibrous habit (VV67b).

extremely fibrous habit and hair-like appearance (Figure 3 a,b). It consists of fleecy fibers having a diameter generally <1 µm and very variable lengths, up to 500-600 µm. The longer fibers seem elastic and flexible and are often grouped in sub-parallel or bent bundles that fray into aggregates of 10-30 µm in diameter. However, it is interesting to note how these fibers are formed by a close association of very thin and curled fibrils that may be as small as 10-15 nm. This morphological type with a woolly aspect is very similar in appearance to the holotype from Durkee, Oregon, USA (Eakle, 1898; Staples and Gard, 1959) and to that from Lander County, Nevada, USA (Mattioli et al., 2016b; Ballirano et al., 2018). Furthermore, a similar habit has also been observed for Italian erionite from Lessini Mounts (Giordani et al., 2017).

In sample VV67b, the erionite occurs as crystals with acicular to highly fibrous habit often gathered in radiated bundles and aggregates of a few tens of millimeters in diameter and variable length up to ~1 mm (Figure 3 c,d). The individual fibers and fibrils always have a diameter <1 µm while their lengths are variable, with maximum observed values of 600 µm. Unlike those of sample VV67a, the fibers of VV67b have a stiffer appearance, are less flexible and tend to gather in small, pointed bundles at the ends of the aggregates (like-brushes terminations). However, although this sample seems to show a more prismatic appearance than VV67a, it also tends to split into very thin fibers and fibrils. This sample is very similar

in appearance to that from Berici Hills, Northern Italy, as described by Giordani et al. (2017).

The microchemical data of the studied samples are given in Table 2. The extremely fibrous, hair-like erionite (VV67a sample) can be classified as erionite-K and its average chemical composition is $(K_{2.68}Ca_{1.86}Na_{0.96}Mg_{0.23})[Al_{8.19}Si_{27.81}O_{72}]\cdot 29.58\ H_2O$. The Si/(Si+Al) average ratio is 0.773, which is slightly higher with respect to the literature interval for the erionite from volcanic rocks (Passaglia et al., 1998) but very similar to the erionites from Durkee, Oregon, USA (Passaglia et al., 1998) and Lander County, Nevada, USA (Mattioli et al., 2016b; Ballirano et al., 2018).

The dominant extra-framework cation in the structure is K^+ (2.56-2.8 *apfu*), while Ca^{2+} and Na^+ contents are generally low (1.77-1.95 and 1.24-0.78 *apfu*, respectively), as well as Mg^{2+} content (0.17-0.29 *apfu*). The Mg/(Ca + Na) ratio, indicated as one of the most significant parameters for the erionite-offretite distinction (Passaglia et al., 1998), is also very low (0.05-0.11) and typical for the species erionite. Iron is not present in the ideal chemical formula and the very small amount of Fe detected in sporadic analysis points (up to 0.02 *apfu*) is more likely due to impurities allocated at the fiber surface.

The water content of the pristine VV67a sample was determined by thermogravimetric analysis (TGA). The TGA curve showed a first main mass loss of 14.83% up to 590 °C and a second minor mass loss of 3.67% between 590 °C and 690 °C, for a total mass loss of 18.45% (Figure 4). In this second reaction, a small part of the water loss

Table 2. SEM-EDS chemical analyses of erionite samples VV67a and VV67b. In addition, data of erionite-Na from Lander County (Nevada, USA) (Mattioli et al., 2016) are reported for comparison.
E% as defined by Passaglia (1970).
*Iron content due to impurities allocated at the fibres surface.

Oxides (wt%)	VV67a	VV67b	Lander County
SiO_2	57.78(25)	52.98(30)	58.47(35)
Al_2O_3	14.43(23)	17.41(42)	14.30(21)
Na_2O	1.02(20)	5.08(22)	0.80(10)
K_2O	4.36(19)	3.67(28)	4.17(29)
MgO	0.32(8)	0.36(8)	0.48(12)
CaO	3.60(16)	2.05(15)	3.35(23)
Fe_2O_3*	0.04(4)	-	0.12(4)
H_2O	18.45	18.45	18.46(45)
Total	100.00	100.00	100.15
Si	27.81(12)	25.95(19)	27.94(10)
Al	8.19(12)	10.05(19)	8.06(12)
Na	0.96(18)	4.82(23)	0.74(10)
K	2.68(12)	2.30(18)	2.55(18)
Mg	0.23(6)	0.26(6)	0.34(9)
Ca	1.86(9)	1.08(8)	1.72(12)
Fe	0.01(1)	-	0.05(2)
O	71.83(14)	71.87(29)	71.72
H_2O	29.58(16)	30.14(20)	29.48(77)
E%	5.09	2.90	7.52
R=Si/(Si+Al)	0.773(3)	0.721(5)	0.776(2)
Total s.s. EF cation (e^-)	101.3(14)	121.0(5)	96.0(9)
M/(M+D)	0.634(18)	0.842(12)	0.609

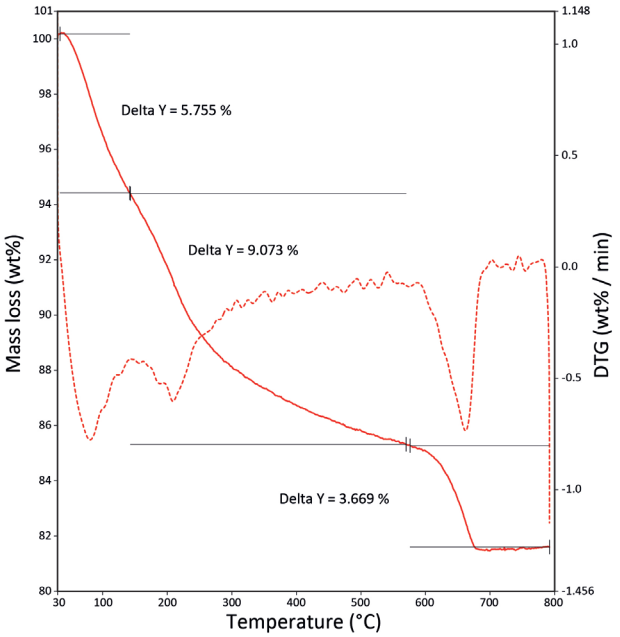

Figure 4. Thermogravimetric curve (TGA, solid line) and its first derivative (DTG, dotted line) of sample VV67a.

(not quantifiable) could also be related to the impurities such as calcite and layer silicates.

Unlike the previous sample, the acicular to highly fibrous erionite (VV67b sample) is classified as erionite-Na and its average composition is $(Na_{4.82}K_{2.30}Ca_{1.08}Mg_{0.26})[Al_{10.05}Si_{25.95}O_{72}]\cdot 30.14\ H_2O$, with a Si/(Si+Al) ratio in the range 0.72-0.73. In this type of erionite, the dominant extra-framework cation is always Na^+(4.59-5.05 *apfu*), with K^+(2.12-2.48 *apfu*) and Ca^{2+}(1.00-1.16 *apfu*) as minor constituents. The Mg^{2+} content is generally low (average 0.26 *apfu*), as well as the Mg/(Ca+Na) ratio (0.03-0.07). Owing to the scarcity of material, no TGA was performed on the sample VV67b; for this reason, it has been used the water content determined in sample VV67a.

Powder X-ray Diffraction (PXRD)

A comparison of the diffraction patterns of the two samples immediately shows the effect of the very different morphological features of the two samples (Figure 5).

In fact, the severe broadening of the peaks experienced by sample VV67a is coherent with its "woolly" morphology, very similar to that observed for a sample of erionite-Na from Durkee (Oregon, USA), characterized by Cametti et al. (2013) and the sample of erionite-Ca BV201 from Lessini Mounts (Italy) described by Giordani

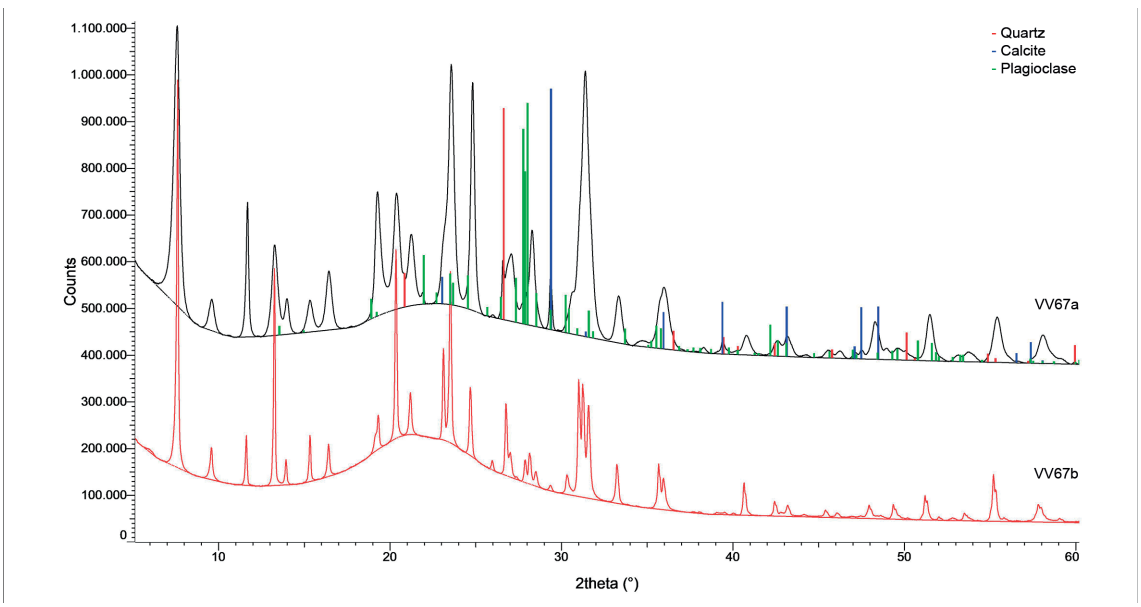

Figure 5. Comparison of the diffraction patterns (magnified view 5-60° 2θ) of the investigated erionite samples VV67a and VV67b. Patterns were vertically displaced to facilitate comparison. Colored vertical bars mark the position of the reflections of quartz, calcite, and plagioclase feldspar occurring in mixture with erionite in sample VV67a. The small reflection at ca. 29.5° 2θ in the diffraction pattern of VV67b indicates the occurrence of calcite.

et al. (2017).

A first refinement was carried out considering the following:

a) man isotropic shape of the crystallites.

The refinement smoothly converged to the following agreement indices: R_{wp}=2.85%, R_p=1.67%, R_B=0.33% (Young, 1993). However, a scrutiny of the Rietveld plots (Figure 6a) indicated an imperfect fitting of the shape of a few peaks due to a marked anisotropic peak broadening arising from the shape/bending of the fibrils. This misfit is particularly evident in the case of the 002 reflection located at ca. 12° 2θ.

Therefore, a series of refinements were performed to model such anisotropy using:

b) the multidimensional distribution of lattice metrics of Stephens (1999) imposing a hexagonal symmetry (Figure 6b);

c) the ellipsoid-model of Katerinopoulou et al. (2012) describing the diffraction-vector dependent broadening of diffraction maxima (Figure 6c). In the hexagonal symmetry, the shape ellipsoid parameters b_{ij} are constrained as $b_{11}=b_{22}=2b_{12}$; $b_{13}=b_{23}=0$. The orientation

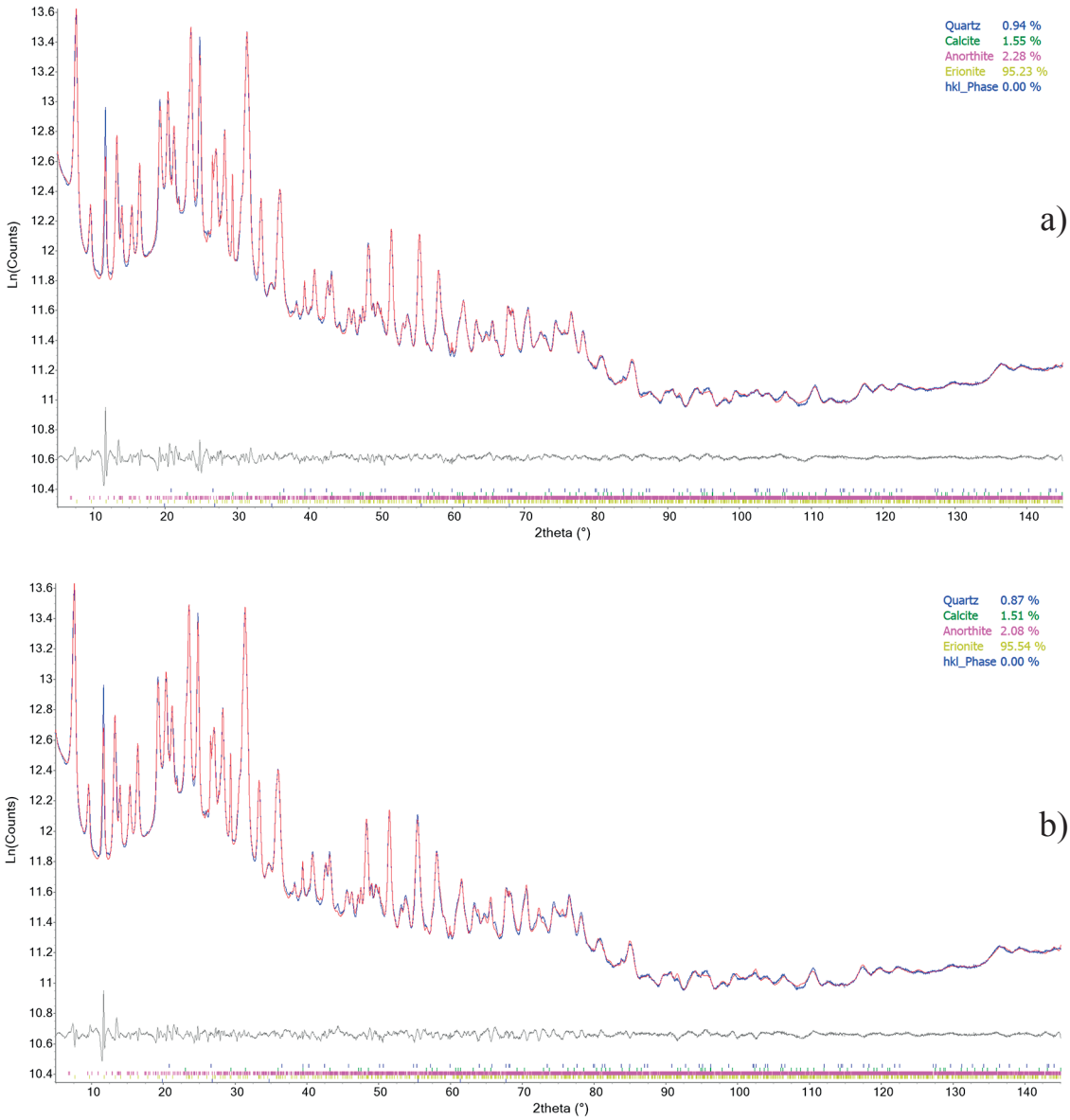

Figure 6 a,b. Final Rietveld plots of the refinements of the investigated erionite sample VV67a, carried out using different approaches to model peak shape. a) Isotropic broadening; b) Stephens (1999) hexagonal anisotropic broadening.

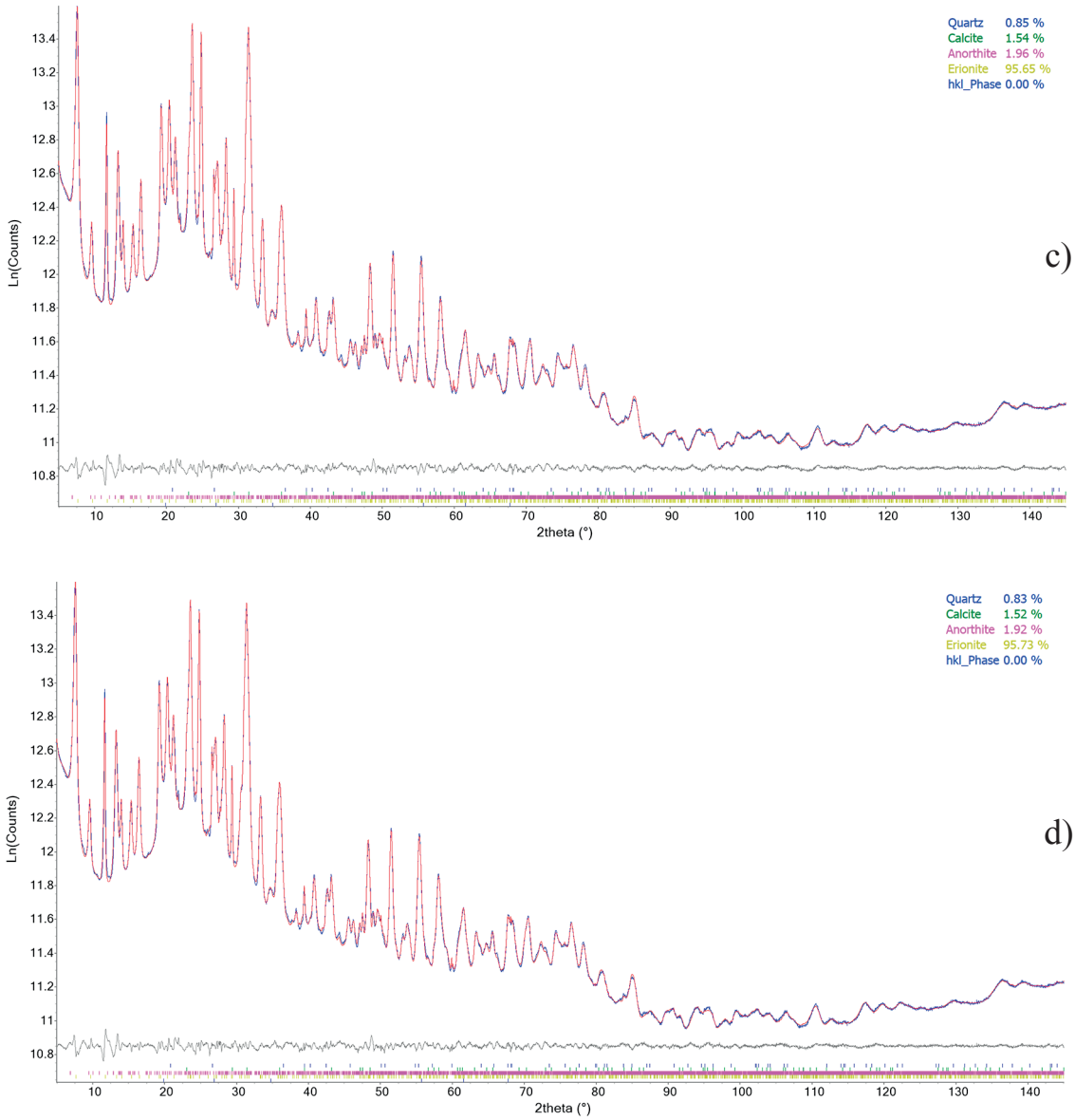

Figure 6 c,d. Final Rietveld plots of the refinements of the investigated erionite sample VV67a, carried out using different approaches to model peak shape. c) ellipsoid model of Katerinopoulou et al. (2012); d) normalized symmetrized spherical harmonics approach of Järvinen (1993). Blue line: experimental; red line: calculated; gray line (below): difference plot. Vertical lines refer to the calculated reflections of (from above to below): quartz, calcite, plagioclase, erionite and phyllosilicate.

of the ellipsoid is such that the principal radii $r_a \perp c$ and $r_c \| c$;

d) the normalized symmetrized spherical harmonic model of Järvinen (1993) for describing the anisotropic peak broadening applied to the Lorentzian half-width (Figure 6d).

A significant, progressive improvement of the fit was obtained by passing from a) to d), which represents the best-performing model, as indicated by the final agreement indices of R_{wp}=1.70%, R_p=1.16%, R_B=0.20%. Both models c) and d) produced similar fittings in terms of residuals, albeit some imperfect fit of the low-angle reflections still persisted.

Differences obtained in the quantitative phase analysis (QPA) among the various refinements indicate a regular, albeit minor, increase of the erionite content because of the improved description of its peak shape.

The following paragraphs will discuss the results

obtained from the d) refinement.

In the case of sample VV67b we followed the same procedure and again the best fit was achieved using the normalized symmetrized spherical harmonic model of Järvinen (Figure 7).

Therefore, the results from the isotropic peak broadening model will be discussed in the following paragraphs. Complete structural data of both samples are available for download as cif files at the journal site. Experimental details and miscellaneous data on the refinements are reported in Table 3.

Structural refinement

Sample VV67a

Calculated cell parameters a=13.2553(3) Å and c= 15.0529(3) Å and cell volume V = 2290.49(11) Å^3 are close to those reported by Mattioli et al. (2016b) and Pacella et al. (2018) for "woolly" erionite-K from Lander County (Nevada, USA), as expected from the very similar R-value and chemistry (Table 3). Moreover, they are also close to those reported by Cametti et al. (2013) for "woolly" erionite-Na from Durkee (Oregon, USA), having a similar R-value.

As a matter of comparison with reference data, we report a few data obtained from the refinement using the ellipsoid-model of Katerinoupoulou et al. (2012) for approximating the anisotropic peak shape. The principal ellipsoid radii of r_a=18.68(16) nm and r_c=75(3) nm were computed from the refined anisotropic crystal shape parameters b_{11} and b_{33}, using the relationships r_a=1/(a cos 30° $b_{11}^{0.5}$) and r_c=1/(c $b_{33}^{0.5}$). Those values lead to a r_c/r_a ratio of 4.0(7). The refined parameters are similar to those reported by Cametti et al. (2013) (r_a=15.5(2) nm and r_c =79(5) nm; r_c/r_a ratio of 5.1(9)) for woolly erionite-Na from Durkee (Oregon, USA) whereas Pacella et al. (2018) report a significantly shorter r_c value of 51.1(18) nm for the erionite-K sample from Lander County (Table 4).

The mean bond distances <T1-O>=1.632 Å and <T2-O>=1.616 Å, obtained from the spherical harmonic model fit, suggest a disordered Si/Al distribution (<T1-O>-<T2-O>=0.016 Å) and the preferential partition of Al at the T1 site, differently from most of the refined structure of erionite samples. A preferential partition of Al at T1 has been reported by Giordani et al. (2017) in sample MB170 from Berici Hills (Italy). It is worth noting that the calculated <T2-O> strongly depends on the anomalously short value of 1.561 Å obtained for T2-O6. The R ratio has been calculated using both the Jones' determinative curves (Jones, 1968) and the regression equation of Giordani et al. (2017). The population of the two T1 ($Al_{4.36}Si_{19.64}$) and T2 ($Al_{0.93}Si_{11.07}$) sites, determined using the Jones' determinative curve, indicates an R-value of 0.853 which significantly exceeds the common range of 0.69-0.79 observed for erionite samples (Passaglia et al., 1998). Differently, an R-value of 0.793 has been obtained using the regression equation of Giordani et al. (2017). The latter value is in reasonable agreement with 0.773(3) from chemical data.

A further refinement (not reported) has been performed imposing soft restraints to the T(1,2)O_4 tetrahedra with individual T-O bond distances set to 1.6385(10) Å and O-O contacts set to 2.675(2) Å, the latter corresponding

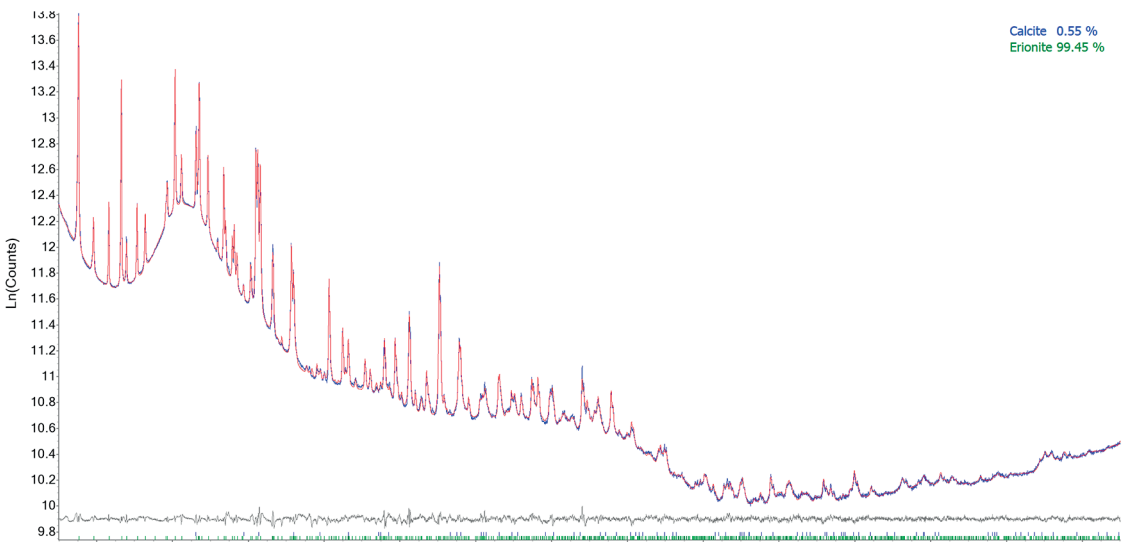

Figure 7. Final Rietveld plots of the refinement of the investigated erionite sample VV67b. Blue line: experimental; red line: calculated; gray line (below): difference plot. Vertical lines refer to the calculated reflections of (from above to below): calcite, erionite.

Table 3. Experimental details and miscellaneous data of the refinements. Layer silicates not quantified. Their presence is indicated with "+". Refinements are coded as follow: a) isotropic broadening; b) Stephens (1999) model; c) Katerinopoulou et al. (2012) model; d) normalized spherical harmonics (Järvinen, 1993); 1) isotropic broadening. Statistic indicators as defined in Young (1993).

	VV67a				**VV67b**
	a)	b)	c)	d)	1)
Instrument	Bruker AXS D8 Advantage				
Radiation	Cu Kα				
Primary and secondary radii (mm)	250				
Sample mount	Rotating capillary (60 r/min)				
Incident beam optics	Focusing Göbel mirror				
Detector window (°)	6				
Angular range (° 2θ)	5-145				
Step size (° 2θ)	0.021798				
Counting time (σ)	40				
R_{wp}	2.849	2.447	1.761	1.699	1.671
R_p	1.671	1.550	1.215	1.164	1.244
R_B	0.334	0.362	0.205	0.197	0.382
GoF	9.758	8.383	6.032	5.822	4.362
DWd	0.097	0.104	0.101	0.105	0.352
QPA					
Erionite (wt%)	95.21(14)	95.54(12)	95.66(9)	95.73(8)	99.45(9)
Plagioclase (wt%)	2.28(10)	2.08(8)	1.96(6)	1.92(6)	-
Calcite (wt%)	1.57(9)	1.51(8)	1.54(6)	1.52(6)	0.55(9)
Quartz (wt%)	0.95(3)	0.88(3)	0.852(19)	0.829(18)	-
Layer silicates	+	+	+	+	-
Erionite cell parameters					
a (Å)	13.2553(5)	13.2553(5)	13.2552(3)	13.2553(3)	13.29232(10)
c (Å)	15.0523(5)	15.0529(4)	15.0535(3)	15.0529(3)	15.1460(2)
V (Å^3)	2290.39(18)	2290.48(17)	2290.53(12)	2290.49(11)	2317.56(5)

Table 4. Comparison of principal ellipsoid radii of woolly erionite samples. Data include those of woolly erionite-Na from Durkee, Oregon (Cametti et al., 2013) and erionite-K from Lander County, Nevada (Pacella et al., 2018).

Sample	r_a (nm)	r_c (nm)	r_c/r_a
VV67a	18.68(16)	75.0(3)	4.0(7)
Durkee	15.50(2)	79.0(5)	5.1(9)
Lander county	18.60(2)	51.1(18)	2.8(6)

to regular tetrahedral angles of 109°44. The T-O restraint value was set by hypothesizing R=0.773 and an equipartition of Al in both T1 and T2. The tetrahedra regularized and the T2-O6 bond distance refined to a more conventional value of 1.586(5) Å, despite a minor increase of R_{wp} from 1.699 to 1.761. This fact clearly indicates that the structural results are affected by the quality of the experimental data and that the model used to cope with the severe anisotropic peak broadening is not perfectly adequate. Moreover, a further reason for the not

wholly satisfactory structural results may be related to the imperfect fit of the plagioclase contribution that was not optimized as a part of the refinement, as well as that of layer silicates.

Table 5 reports the fractional coordinates, displacement parameters (B_{iso}), site scattering from refinement (*s.s.* ref.), site scattering from site partition (*s.s.* part.), expressed as e^-, of EF cations and water molecules of both VV67 samples.

Chemical data of VV67a indicate a total site scattering of 101.3(14) e^- for the EF cations. This value is in excellent agreement with the total EF *s.s.* of 103(2) e^- obtained from the Rietveld refinement (Table 2). Similarly, a total of 33.4(15) water molecules *pfu* has been obtained from the

Table 5. Fractional coordinates, isotropic displacement parameters (Biso), site scattering from refinement (s.s. ref.), site scattering from site partition (*s.s.* part.), expressed as e-, of EF cations and water molecules of VV67a and VV67b samples.

	VV67a						
Site	*x*	*y*	*z*	B_{iso}	*s.s.* ref.	site partition	*s.s.* part.
Ca1	1/3	2/3	0.9285(14)	12.60(4)	32.2(6)	$Mg_{0.23}Na_{0.96}Ca_{0.68}$	26.9
Ca2	1/3	2/3	0.1036(15)	12.60(4)	20.8(7)	$Ca_{0.80}$	16.0
Ca3	1/3	2/3	0.6830(4)	12.60(4)	12.2(8)	$Ca_{0.38}$	7.6
K1	0	0	¼	2.14(16)	38.0	$K_{2.00}$	38.0
$S_{EF\ cations}$					103.0(2)		88.5
OW7	0.244(2)	2*x*	¾	6.30(2)	21.0(3)	$K_{0.68}$	12.9
OW8	0.2576(8)	2*x*	0.0203(16)	12.60(4)	54.3(10)		
OW9	0.4333(13)	2*x*	0.9940(2)	12.60(4)	41.0(15)		
OW10	0.253(2)	2*x*	0.6970(3)	12.60(4)	70.2(13)		
OW11	0.4260(8)	2*x*	0.6281(13)	12.60(4)	44.0(4)		
OW12	0.500(3)	2*x*	-0.0300(2)	12.60(4)	37.1(10)		
$S_{water\ mol.}$					267.0(12)		
	VV67b						
Site	*x*	*y*	*Z*	B_{iso}	s.s. ref.	partition	s.s. ref.
Ca1	1/3	2/3	0.8900(3)	15.20(3)	22.4(7)	$Mg_{0.26}Na_{1.36}Ca_{0.29}$	23.9
Ca2	1/3	2/3	0.1248(12)	15.20(3)	41.0(5)	$Na_{3.46}Ca_{0.19}$	41.9
Ca3	1/3	2/3	¾	15.20(3)	10.9(7)	$Ca_{0.60}$	12.0
K1	0	0	¼	2.37(15)	38.0	$K_{2.00}$	38.0
K2	½	0	0	2.37(15)	16.9(9)	$K_{0.30}$	5.7
$S_{EF\ cations}$					129.0(3)		121.5
OW7	0.2287(1)	2*x*	¾	7.60(14)	40.0(3)		
OW8	0.2587(7)	2*x*	-0.0060(2)	15.20(3)	53.3(8)		
OW9	0.4282(17)	2*x*	0.9630(5)	15.20(3)	49.0(3)		
OW10	0.257(3)	2*x*	0.7010(6)	15.20(3)	29.0(2)		
OW11	0.4344(8)	2*x*	0.6552(19)	15.20(3)	59.3(17)		
OW12	0.4518(17)	2*x*	0.0360(4)	15.20(3)	45.0(4)		
$S_{water\ mol.}$					276.0(17)		

refinement, slightly higher than 29.6 water molecules *pfu* from TGA measurements.

The position of the EF cation sites is close to that of the Lander County sample (Pacella et al., 2018) as well as the refined EF *s.s.* As a further similarity, no site scattering was observed at the K2 site despite the evidence from SEM-EDS of additional K allocated into the erionite cage. However, the position of OW12 is very close to ½ 0 0 (i.e., the K2 site located at the center of the boat-shaped 8-member rings (8MR) forming the walls of the erionite cage), suggesting that the refined position of OW12 reflects, in effect, the inability to separate two close sites from the present experimental data. However, if the additional 0.30 *apfu* K are allocated at K2 we observe an excess of refined *s.s.* at the Ca1, Ca2, and Ca3 cation sites compared to SEM-EDS analysis. This fact may be explained in several ways:

a) alkali loss during SEM-EDS analysis (Pacella et al., 2016);

b) the distribution of the additional K into one or more EF cation sites allocated along the axis of the erionite cage;

c) an artifact caused by the imperfect modeling of the anisotropic peak shape.

In Table 5, such excess has been tentatively distributed equally among Ca1, Ca2 and Ca3.

Sample VV67b

Calculated cell parameters are *a*=13.29189(10) Å and *c* =15.1456(2) Å and cell volume V=2317.35(5) Å^3. They are larger than VV67a, pointing to a smaller R-value. Moreover, the standard deviation of the *c*-parameter is double than that of the *a*-parameter, whereas they are consistently found to be equal. This fact could suggest the possible occurrence of some degree of stacking disorder along the *c*-axis that is commonly found in erionite (Kokotailo et al., 1972). Therefore, we have explored such possibility, including the framework of erionite extra-rings mimicking the occurrence of offretite type stacking faults, as shown in Schlenker et al. (1977), and permitting the refinement of the fraction of such faults. However, any attempt to include such a model in the refinement failed, possibly due to a very low population of faults. An alternative explanation of the larger standard deviation of the *c*-parameter than that of the *a*-parameter could be related to the effect of the occurrence in a mixture of minor VV67a.

The mean bond distances <T1-O> = 1.643 Å and <T2-O>=1.638 Å indicate a disordered Si/Al distribution (<T1-O>-<T2-O>=0.005 Å) with a slight preferential partition of Al at the T1 site. The population of the T1 ($Al_{6.09}Si_{25.91}$) and T2 ($Al_{2.60}Si_{9.40}$) sites, determined using the Jones' determinative curve, provides an R-value of 0.758. Differently, an R-value of 0.726 has been obtained using the regression equation of Giordani et al. (2017). The latter value is in excellent agreement with 0.721(5) obtained from chemical data.

Isotropic displacement parameters (B_{iso}) of oxygen atoms of the framework (Table 5) are more significant than those commonly observed in other refinements of erionite structure, possibly confirming the occurrence of some stacking disorder.

SEM-EDS analysis of VV67b indicates a total site scattering of 121(4) e$^-$ for the EF cations, in good agreement with the *s.s.* of 129(3) e$^-$ obtained from the Rietveld refinement (Table 2). A tentative cation partition is also reported in Table 5. According to the refinement, the largest misfit is related to the K content that should exceed the value obtained from SEM-EDS analysis. As suggested in the case of VV67a, such difference could be justified by alkali loss during SEM-EDS analysis or by artifacts arising from the presence of stacking disorder. A total of 34(2) water molecules *pfu* has been obtained from the refinement, but, owing to the scarcity of material, no TGA was performed on the sample. This value is somewhat higher than commonly observed in erionite samples (Coombs et al., 1997; Armbruster and Gunter, 2001).

Vibrational (FTIR and Raman) spectroscopy

The μ-FTIR spectrum in the O-H stretching region of Vico erionite (sample VV67a), collected on a very small bundle of extremely fibrous crystals, is displayed in Figure 8. It shows a very broad and convolute absorption extending from 2500 to 3700 cm^{-1} and peaked at ~3380 cm^{-1} which is evidently due to the overlapping of several components. A very intense band at 1631 cm^{-1} (Figure 8) is assigned to the bending mode of H_2O. The triplet of sharp peaks at 3000-2800 cm^{-1} is assigned to C-H modes due to the pollution of grease used to handle the sample. The weak and broad absorption at 5213 cm^{-1} in the FIR (Far InfraRed) region is due to the combination of stretching and bending ($\nu_{OH}+\delta_{OH}$) modes of the H_2O/OH molecules. This latter peak is well resolved in a spectrum collected on a thicker part of the sample (inset in Figure 8), where the absorption in the MIR range is evidently out of scale; this pattern excludes any presence of hydroxyl groups in the structure whose combination frequencies typically occur at between 4000 and 4500 cm^{-1} (Della Ventura et al., 2009).

The absorption in the 3800-2400 cm^{-1} range has been tentatively decomposed by fitting the smallest number of Gaussian bands while leaving both positions and FWHMs (full width at half maximum height) unconstrained. The result shows that the pattern can be well reproduced using five peaks centered at 3630, 3563, 3451, 3265 and 2990

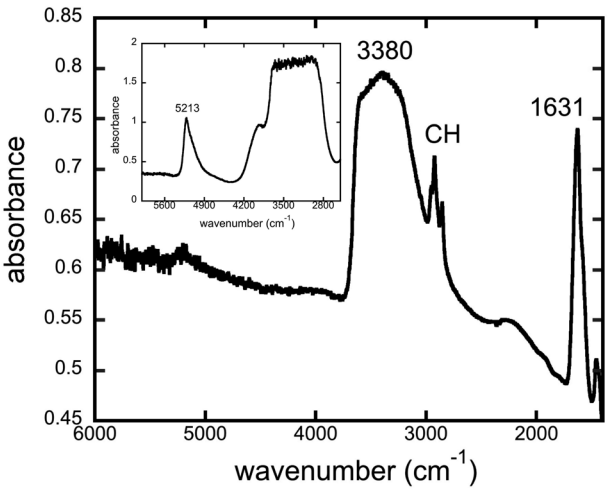

Figure 8. Selected FTIR spectrum of the investigated erionite sample VV67a, collected on a very small bundle of extremely fibrous crystals. The inset shows the spectrum collected on a thicker part of the sample.

cm^{-1}, respectively (Figure 9a). The first three peaks are due to O-H stretching modes of the H_2O molecules in the erionite cages, while the broad component at 3265 cm^{-1} can be confidently assigned to the first overtone of the H_2O bending mode ($2\times d_{OH}$); the broad absorption at 2990 cm^{-1} is necessary to model the strong asymmetry of the broad band.

A selected Raman spectrum of erionite from Vico is presented in Figure 10. It shows a very intense broad and asymmetric peak at 3459 cm^{-1} in the principal OH-stretching region and a series of scattering peaks in the low-frequency range (<1200 cm^{-1}). The most intense feature is a doublet at 470-485 cm^{-1} that is assigned to the T-O-T bending mode (Croce et al., 2013; Giacobbe et al., 2023); weaker scatterings are observed at 1102-1135 cm^{-1} (T-O antisymmetric stretching mode), at 779-811, 560 and 342 cm^{-1}. Finally, the relatively intense peak at 134 cm^{-1} can be assigned to a lattice mode of the zeolite structure. The described pattern is almost identical to previous data reported in the literature for erionite (Croce et al., 2013; Rinaudo and Croce, 2019) and excludes any presence of other phases, particularly offretite associated with the studied zeolite (Giacobbe et al., 2023). The Raman pattern in the 3800-2400 cm^{-1} range has been decomposed in the same way as the FTIR spectrum and the result shows five peaks centered at 3623, 3553, 3442, 3273 and 3020 cm^{-1}, respectively (Figure 9b). Again, the first three components can be assigned to O-H stretching modes. Therefore, the FTIR and Raman spectra in the principal OH-stretching range are similar and show the same multiplicity of peaks at almost the same wavenumbers,

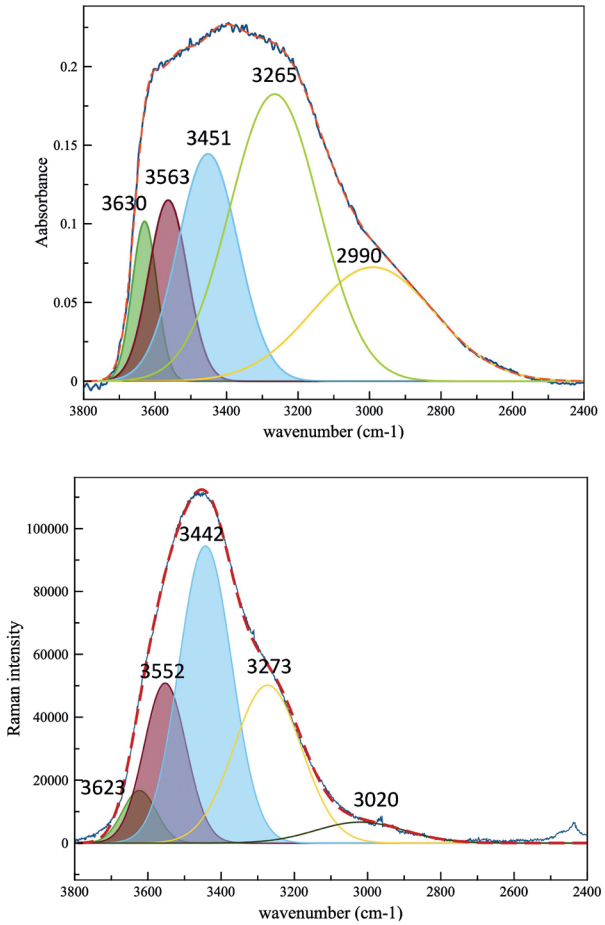

Figure 9. Decomposed (a) FTIR and (b) Raman spectra of the investigated erionite sample VV67a in the principal OH-stretching region (3800-2400 cm-1). The single Gaussian components are highlighted by different colors; the experimental pattern is in blue, while the sum curve resulting from the fitting is indicated with a red dashed line.

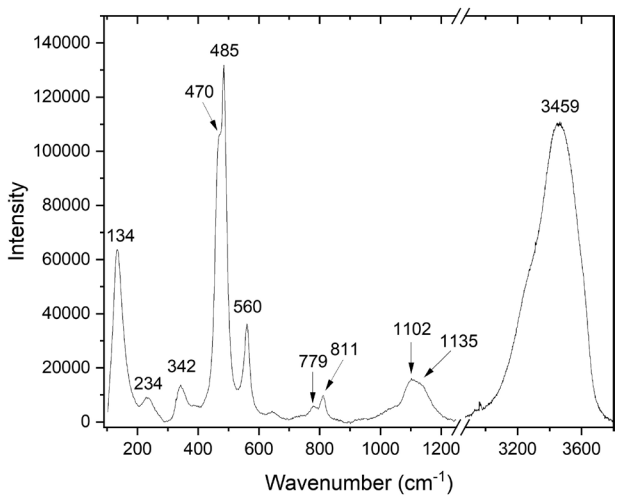

Figure 10. Selected Raman spectrum of the investigated erionite sample VV67a.

only their relative intensities being different. Infrared data on erionite are very scarce in the literature and collected only on KBr pellets (Best et al., 1973; Roessner et al., 1987) on ammonia or D_2O-exchanged zeolites. Best et al. (1973) show spectra consisting of a doublet of well-separated peaks at 3612 and 3565 cm^{-1} that correspond well with the two higher-wavenumber components in our fittings.

CONCLUSIONS

This study reports a detailed crystal-chemical and structural characterization of erionite, a carcinogenic fibrous zeolite recently discovered for the first time in the volcanic rocks of Latium, Italy. Our results, based on a multi-methodological approach, can be summarized as follow.

- There are two types of erionite, both of hydrothermal origin, that coexist within the same host-rock but significantly differ in terms of morphology, crystal chemistry and structure.

- The first type (VV67a) is an erionite-K with an extremely fibrous habit and a woolly appearance showing a great tendency to separate in very thin and curled fibrils. The calculated cell parameters are *a*=13.2553(3) Å, *c*= 15.0529(3) Å and cell volume V= 290.49(11) $Å^3$.

- The second type (VV67b) is an erionite-Na characterized by acicular to highly fibrous habit with stiffer appearance and rigid behavior, also in this case willing to divide into thin fibrils. Its calculated cell parameters appear larger than the previous type and are *a*=13.29189(10) Å, *c*=15.1456(2) Å and cell volume V= 2317.35(5) $Å^3$.

- The structure of both samples is consistent with that of samples with similar composition. However, details of the mutual EF cations/H_2O molecules arrangement are missing owing to the difficulty to model the anisotropic behavior of the peak-shape, which is very impactful, especially for VV67b.

- The μ-FTIR and Raman spectra in the O-H stretching region are similar in terms of band multiplicity and show three component bands around 3630, 3560 and 3450 cm^{-1} due to the H_2O molecules in the structural cages. The Raman spectrum in the lattice region (<1200 cm^{-1}) is identical to previous spectra reported in the literature.

Finally, it is essential to make an important consideration on human health. The presence of zeolites in the volcanic rocks from Latium is well known, but the species reported so far are all non-fibrous zeolites (mainly chabazite and phillipsite). This new occurrence of carcinogenic fibrous erionite in lithologies that are often extensively quarried and widely employed raises an important question on the risk assessments. Given the wide extension of these volcanic rocks, the possibility of environmental and professional exposure to this hazardous fibrous zeolite cannot be overlooked, considering also the occurrence of another fibrous mineral (tremolite) in the same type of rocks as reported by Della Ventura et al. (2014).

ACKNOWLEDGEMENTS

This research was conducted within the research project "Fibres, A Multidisciplinary Mineralogical, Crystal-Chemical and Biological Project to Amend the Paradigm of Toxicity and Cancerogenicity of Mineral Fibres" (Code PRIN20173X8WA4). We warmly thank Eleonora Macedi and Laura Valentini for their kind assistance during the TGA-DSC analyses and the acquisition of SEM images, respectively. The useful comments of two anonymous reviewers are also greatly appreciated.

REFERENCES

Angel R.J., Carpenter M.A., Finger L.W., 1990. Structural variation associated with compositional variation and order-disorder behavior in anorthite-rich feldspars. American Mineralogist 75, 150-162

Armbruster T. and Gunter M.E., 2001. Crystal structures of natural zeolites. In: Bish D.L., Ming D.W. (Eds.), Natural Zeolites: Occurrence, Properties, Applications; Reviews in Mineralogy and Geochemistry, vol. 45. Mineralogical Society of America, Washington, DC, USA, 1-67. doi: 10.2138/rmg.2001.45.1.

Ballirano P., 2003. Effects of the choice of different ionization level for scattering curves and correction for small preferred orientation in Rietveld refinement: the $MgAl_2O_4$ test case. Journal of Applied Crystallography 36, 1056-1061. doi: 10.1107/S0021889803010410.

Ballirano P., 2011. Laboratory parallel-beam transmission X-ray powder diffraction investigation of the thermal behavior of nitratine $NaNO_3$: spontaneous strain and structure evolution. Physics and Chemistry of Minerals, 38, 531-541. doi: 10.1007/s00269-011-0425-4.

Ballirano P. and Maras A., 2006. Mineralogical characterization of the blue pigment of Michelangelo's fresco "The Last Judgment". American Mineralogist 91, 997-1005. doi: 10.2138/am.2006.2117

Ballirano P., Pacella A., Cremisini C., Nardi E., Fantauzzi M., Atzei D., Rossi A., Cametti G., 2015. Fe (II) segregation at a specific crystallographic site of fibrous erionite: A first step toward the understanding of the mechanisms inducing its carcinogenicity. Microporous and Mesoporous Material 211, 49-63.

Ballirano P., Bloise A., Gualtieri A.F., Lezzerini M., Pacella A., Perchiazzi N., Dogan M., Dogan A.U., 2017. The crystal structure of mineral fibres. In Mineral Fibres: Crystal Chemistry, Chemical-Physical Properties, Biological Interaction and Toxicity; Gualtieri A.F., Ed.; EMU Notes in Mineralogy; European Mineralogical Union and Mineralogical Society of Great Britain & Ireland: London,

UK, 2017; Volume 18, 17-64.

Ballirano P., Pacella A., Bloise A., Giordani M., Mattioli M., 2018. Thermal stability of woolly erionite-K and considerations about the heat-induced behaviour of the erionite group. Minerals 8 (1), 28. doi: 10.3390/min8010028.

Best D.F., Larson R.W., Angell C.L.,1973. Infrared spectroscopic investigation of zeolites and adsorbed molecules. VII. Hydroxyl groups in erionite. Journal of Physical Chemistry 77, 2183-2185.

Bruker AXS, 2016. Topas V6: General Profile and Structure Analysis Software for Powder Diffraction Data; Bruker AXS: Karlsruhe, Germany.

Cametti G., Pacella A., Mura F., Rossi M., Ballirano P., 2013. New morphological, chemical, and structural data of woolly erionite-Na from Durkee, Oregon, U.S.A. American Mineralogist 98, 2155-2163.

Cangiotti M., Salucci S., Battistelli M., Falcieri E., Mattioli M., Giordani M., Ottaviani M.F., 2018. EPR, TEM and cell viability study of asbestiform zeolite fibers in cell media. Colloids and Surfaces B: Biointerfaces 161, 147-155. doi: 10.1016/j.colsurfb.2017.10.045.

Carbone M., Adusumilli P.S., Alexander Jr. H.R., Baas P., Bardelli F., Bononi A., Bueno R., Felley-Bosco E., Galateau-Salle F., Jablons D., Mansfield A.S., 2019. Mesothelioma: scientific clues for prevention, diagnosis, and therapy. CA: A Cancer Journal of Clinicians 69, 402-429. doi: 10.3322/caac.21572.

Carbone M., Baris Y.I., Bertino P., Brass B., Comertpay S., Dogan A.U., Gaudino G., Jube S., Kanodia S., Partridge C.R., Pass H.I., Rivera Z.S., Steele I., Tuncer M., Way S., Yang H., Miller A., 2011. Erionite exposure in North Dakota and Turkish villages with mesothelioma. Proceedings of the National Academy of Sciences 108, 13618-13623. doi: 10.1073/pnas.1105887108

Cardile V., Renis M., Scifo C., Lombardo L., Gulino R., Mancari B., Panico A., 2004. Behaviour of the new asbestos amphibole fluoro-edenite in different lung cell systems. International Journal of Biochemistry and Cell Biology 36, 849-860. doi: 10.1016/j. biocel.2003.09.007.

Cardile V., Lombardo L., Belluso E., Panico A., Capella S., Balazy M., 2007. Toxicity and carcinogenicity mechanisms of fibrous antigorite. International Journal of Environmental Research and Public Health 4, 1-9. doi: 10.3390/ijerph2007010001.

Carr A. and Frey B. 1999. Does vitamin C act as a pro-oxidant under physiological conditions? FASEB Journal 13, 1007-1023.

Cheary R.W. and Coelho A., 1992. A fundamental parameters approach to X-ray line-profile fitting. Journal of Applied Crystallography 25, 109-121. doi: 10.1107/s0021889891010804

Coffin D.L., Cook P.M., Creason J.P., 1992. Relative Mesothelioma Induction in Rats by Mineral Fibers: Comparison with Residual Pulmonary Mineral Fiber Number and Epidemiology. Inhalation Toxicology 4, 273-300. doi: 10.3109/08958379209145671.

Comba P., Gianfagna, A., Paoletti, L., 2003. Pleural mesothelioma cases in Biancavilla are related to a new fluoro-edenite fibrous amphibole. Archives of Environmental and Occupational Health 58, 229-232. doi: 10.3200/AEOH.58.4.229-232.

Conticelli S., Avanzinelli R., Poli G., Braschi E., Giordano G., 2013. Shift from lamproite-like to leucititic rocks: Sr–Nd–Pb isotope data from the Monte Cimino volcanic complex vs. the Vico stratovolcano, Central Italy. Chemical Geology 353, 246-266.

Coombs, D.S., Alberti A., Armbruster T., Artioli G., Colella C., Galli E., Grice J.D., Liebau F., Mandarino J.A., Minato H., Nickel E.H., Passaglia E., Peacor D.R., Quartieri S., Rinaldi R., Ross M., Sheppard R. A., Tillmanns E., Vezzalini G., 1997. Recommended nomenclature for zeolite minerals: Report of the subcommittee on zeolites of the International Mineralogical Association, Commission on New Minerals and Mineral Names. Canadian Mineralogist 35, 1571-606.

Croce A., Musa M., Allegrina M., Rinaudo C., Izzettin Baris Y., Umran Dogan A., Powers A., Rivera Z., Bertino P., Yang H., Gaudino G., Carbone M., 2013. Micro-Raman spectroscopy identifies crocidolite and erionite fibers in tissue sections. Journal of Raman Spectroscopy 44, 1440-1445.

Della Ventura G., Gatta D., Redhammer G., Bellatreccia F., Loose A., Parodi G.C., 2009. Single-crystal polarized FTIR spectroscopy and neutron diffraction refinement of cancrinite. Physics and Chemistry of Minerals 36, 193-206.

Della Ventura, G., Mottana, A., Caprilli, E., Bellatreccia, F., De Benedetti, A., 2014. Asbestiform tremolite within the late pyroclastic deposits of the Alban Hills volcano (Latium, Italy): FTIR spectroscopy and crystal chemistry. Rendiconti Accademia Lincei 25, 229-236. doi: 10.1007/s12210-013-0283-8

Di Giuseppe D., 2020. Characterization of Fibrous Mordenite: A First Step for the Evaluation of its Potential Toxicity. Crystals 10(9), 769. doi: 10.3390/cryst10090769.

Di Giuseppe D., Harper M., Bailey M., Erskine B., Della Ventura G., Ardit M., Pasquali L., Tomaino G., Ray R., Mason H., Dyar M.D., 2019. Characterization and assessment of the potential toxicity/pathogenicity of fibrous glaucophane. Environmental Researches 178, 108723. doi: 10.1016/j.envres.2019.108723.

Dogan A.U. and Dogan M., 2008. Re-evaluation and re-classification of erionite series minerals. Environmental Geochemistry and Health 30, 355-366. doi: 10.1007/s10653-008-9163-z.

Dogan A.U., Dogan M., Hoskins J.A., 2008. Erionite series minerals: mineralogical and carcinogenic properties. Environmental Geochemistry and Health 30, 367-381. doi: 10.1007/s10653-008-9165-x.

Eakle A.S., 1898. Erionite, a new zeolite, American Journal of Science 6, 66-68.

Eborn S.K. and Aust A.E., 1995. Effect of iron acquisition

on induction of DNA singlestrand breaks by erionite, a carcinogenic mineral fiber. Archives of Biochemistry and Biophysics 316, 507-514.

Erskine B.G. and Bailey M., 2018. Characterization of asbestiform glaucophane-winchite in the franciscan complex blueschist, northern diablo range, California. Toxicology and Applied Pharmacology 361, 3-13.

Fach E., Kristovich R., Long J., Waldman W.J., Dutta, P.K., Williams M., 2003. The effect of iron on the biological activities of erionite and mordenite. Environment International 29, 451-458.

García-Romero E. and Suarez M., 2013. Sepiolite-palygorskite: textural study and genetic considerations. Applied Clay Sciences 86, 129-144. doi: 10.1016/j.clay.2013.09.013.

Giacobbe C., Moliterni A., Di Giuseppe D., Malferrari D., Wright J.P., Mattioli M., Raneri S., Giannini C., Fornasini L., Mugnaioli E., Ballirano P., Gualtieri A.F., 2023. The crystal structure of the killer fibre erionite from Tuzköy (Cappadocia, Turkey). International Union of Crystallography Journal 10/4. doi: 10.1107/S2052252523003500.

Gianfagna A., Ballirano P., Bellatreccia F., Bruni B., Paoletti L., Oberti R., 2003. Characterization of amphibole fibres linked to mesothelioma in the area of Biancavilla, Eastern Sicily, Italy. Mineralogical Magazine 67, 1221-1229. doi: 10.1180/0026461036760160.

Giordani M., Mattioli M., Dogan M., Dogan A.U., 2016. Potential carcinogenic erionite from Lessini Mounts, NE Italy: morphological, mineralogical and chemical characterization. Journal of Toxicology and Environmental Health, Part A: Current Issues 79, 808-824. doi: 10.1080/15287394.2016.1182453.

Giordani M., Mattioli M., Ballirano P., Pacella P., Cenni M., Boscardin M., Valentini L., 2017. Geological occurrence, mineralogical characterization and risk assessment of potentially carcinogenic erionite in Italy. Journal of Toxicology and Environmental Health, part B: Critical Reviews 20, 81-103.

Giordani M., Cametti G., Di Lorenzo F., Churakov S.V., 2019. Real-time observation of fibrous zeolites reactivity in contact with simulated lung fluids (SLFs) obtained by atomic force microscope (AFM). Minerals 9, 83. doi: 10.3390/min9020083.

Giordani M., Ballirano P., Pacella A., Meli M.A., Roselli C., Di Lorenzo F., Fagiolino I., Mattioli M., 2022a. Another Potentially Hazardous Zeolite from Northern Italy: Fibrous Mordenite. Minerals 12, 627.

Giordani M., Mattioli M., Cangiotti M., Fattori A., Ottaviani M.F., Betti M., Ballirano P., Pacella A., Di Giuseppe D., Scognamiglio V., Hanuskova M., 2022b. Characterisation of potentially toxic natural fibrous zeolites by means of electron paramagnetic resonance spectroscopy and morphological-mineralogical studies. Chemosphere 291, 133067.

Giordani M., Meli M.A., Roselli C., Betti M., Peruzzi F., Taussi M., Valentini L., Fagiolino I., Mattioli M., 2022c. Could soluble minerals be hazardous to human health? Evidence from fibrous epsomite. Environmental Research 206, 112579.

Giovagnoli L., Boscardin M., 1979. Ritrovamento di levyna ed erionite a Montecchio Maggiore (Vicenza). Rivista Mineralogica Italiana 1, 44-45.

Goldstein J.I., Newbury D.E., Echlin P., Joy D.C., Romig A.D., Lyman C.E., Fiori C., Lifshin E., 1992. Scanning Electron Microscopy and X-Ray Microanalysis, second ed. Plenum Press, New York, NY. doi: 10.1007/978-1-4613-0491-3.

Gottardi G., Galli E., 1985. Natural Zeolites. Springer-Verlag, Berlin. doi: 10.1007/978-3-642-46518-5.

Groppo C., Tomatis M., Turci F., Gazzano E., Ghigo D., Compagnoni R., Fubini B., 2005. Potential toxicity of nonregulated asbestiform minerals: balangeroite from the western Alps. Part 1: identification and characterization. Journal of Toxicology and Environmental Health, Part A 68 (1), 1-19. doi: 10.1080/15287390590523867.

Gualtieri A.F. (Ed.), 2017. Mineral fibres: crystal chemistry, chemical-physical properties, biological interaction and toxicity, 18. European Mineralogical Union and the Mineralogical Society of Great Britain & Ireland, pp. 536.

Gualtieri A.F., 2018. Towards a quantitative model to predict the toxicity/pathogenicity potential of mineral fibers. Toxicology and applied pharmacology 361, 89-98.

Gualtieri A.F., 2021. Bridging the gap between toxicity and carcinogenicity of mineral fibres by connecting the fibre crystal-chemical and physical parameters to the key characteristics of cancer. Current Research in Toxicology 2, 42-52.

Gualtieri A.F., 2023. Journey to the Centre of the Lung. The Perspective of a Mineralogist on the Carcinogenic Effects of Mineral Fibres in the Lungs. Journal of Hazardous Materials, 130077.

Gualtieri A.F., Bursi Gandolfi N., Pollastri S., Pollok K., Langenhorst F., 2016. Where is iron in erionite? A multidisciplinary study of fibrous erionite-Na from Jersey (Nevada, USA). Scientific Report 6, 37981.

Gualtieri A.F., Gandolfi N.B., Passaglia E., Pollastri S., Mattioli M., Giordani M., Ottaviani M.F., Cangiotti M., Bloise A., Barca D., Vigliaturo R., 2018. Is fibrous ferrierite a potential health hazard? Characterization and comparison with fibrous erionite. American Mineralogist 103, 1044-1055.

Gualtieri A.F., Zoboli A., Filaferro M., Benassi M., Scarfì S., Mirata S., Avallone R., Vitale G., Bailey M., Harper M., Di Giuseppe D., 2021. In vitro toxicity of fibrous glaucophane. Toxicology 454, 152743. doi: 10.1016/j.tox.2021.152743.

Gualtieri A.F., Leoncini M., Fantone S., Di Valerio S., Tossetta G., Procopio A.D., Marzioni D., Pugnaloni A., Bassi A.M., Almonti A., Mirata S., Vernazza S., Tirendi S., Marengo B., Traverso N., Passalacqua M., Scarfì S., Raneri S., Fornasini L., Bersani D., Perchiazzi N., Ballirano P., Pacella A., Bloise A., Ottaviani M.F., Mattioli M., Giordani M., Della Ventura G., 2023. PRIN 2017 Fibres - A Multidisciplinary

Mineralogical, Crystal-Chemical and Biological Project. What have we learned after four years of research? Periodico di Mineralogia, this volume.

IARC, 2012. Asbestos (chrysotile, amosite, crocidolite, tremolite, actinolite and anthophyllite), Arsenic, Metals, Fibres and Dusts. International Agency for Research on Cancer.

ICDD, 2021. International Centre for Diffraction Data PDF-2, release 2021.

Ilgren E.B., Kazemian H., Hoskins J.A., 2015. Kandovan the next 'Cappadocia'? A potential public health issue for erionite related mesothelioma risk. Epidemiology, Biostatistics and Public Health 12, 1-12.

Järvinen M., 1993. Application of symmetrized harmonics expansion to correction of the preferred orientation effect. Journal of Applied Crystallography 26, 525-531.

Jones J.B., 1968. Al-O and Si-O tetrahedral distances in aluminosilicate framework structures. Acta Crystallographica Section B Structural Crystallography and Crystal Chemistry 24, 355-58. doi: 10.1107/S0567740868002360.

Katerinopoulou A., Balic-Zunic T., Lundegaard L.F., 2012. Application of the ellipsoid modeling of the average shape of nanosized crystallites in powder diffraction. Journal of Applied Crystallography 45, 22-27.

Kokotailo G.T., Sawruk S., Lawton S.L., 1972. Direct observation of staking faults in the zeolite erionite. American Mineralogist 57, 439-444.

Larson D., Powers A., Ambrosi J.P., Tanji M., Napolitano A., Flores E.G., Baumann F., Pellegrini L., Jennings C.J., Buck B.J., McLaurin B.T., 2016. Investigating palygorskite's role in the development of mesothelioma in southern Nevada: insights into fiber-induced carcinogenicity. Journal of Toxicology and Environmental Health, Part B 19, 213-230. doi: 10.1080/10937404.2016.1195321.

Le Page Y. and Donnay G., 1976. Refinement of the crystal structure of low-quartz. Acta Crystallographica B32, 2456-2459.

Locardi E., 1965. Tipi di ignimbriti di magmi mediterranei. Le ignimbriti del vulcano di Vico. Atti della Società Toscana di Scienze Naturali 72, 55-173.

Matassa R., Famigliari G., Relucenti M., Battaglione E., Downing C., Pacella A., Cametti G., Ballirano P., 2015. A deep look into erionite fibres: An electron microscopy investigation of their self-assembly. Scientific Reports 5, 16757.

Mattioli M., Cenni M., Passaglia E., 2016a. Secondary mineral assemblages as indicators of multistage alteration processes in basaltic lava flows: evidence from the Lessini Mountains, Veneto Volcanic Province, Northern Italy, Periodico di Mineralogia 85, 1-24. doi: 10.2451/2015PM0375.

Mattioli M., Giordani M., Dogan M., Cangiotti M., Avella G., Giorgi R., Dogan A.U., Ottaviani M.F., 2016b. Morpho-chemical characterization and surface properties of carcinogenic zeolite fibers. Journal of Hazardous Material 306, 140-148.

Mattioli M., Giordani M., Arcangeli P., Valentini L., Boscardin M., Pacella A., Ballirano P., 2018. Prismatic to asbestiform offretite from Northern Italy: occurrence, morphology and crystal-chemistry of a new potentially hazardous zeolite. Minerals 8, 69. doi: 10.3390/min8020069.

Mattioli M., Ballirano P., Pacella A., Cangiotti M., Di Lorenzo F., Valentini L., Meli M.A., Roselli C., Fagiolino I., Giordani M., 2022. Fibrous Ferrierite from Northern Italy: Mineralogical Characterization, Surface Properties, and Assessment of Potential Toxicity. Minerals 12, 626.

Nappi G., Chiocchini U., Mattioli M., Valentini L., 2016. Note Illustrative del Foglio 355 Ronciglione della Carta Geologica d'Italia alla scala 1:50.000. Roma, ISPRA, 156 pp.

Novembre D., Gimeno D., Cappelletti P., Graziano S.F., 2021. A case study of zeolitization process: "Tufo Rosso a Scorie Nere" (Vico volcano, Italy): inferences for a general model. European Journal of Mineralogy, 33, 315-328. doi: 10.5194/ejm-33-315-2021

Ortega-Guerrero M.A., Carrasco-Nuñez G., 2014. Environmental occurrence, origin, physical and geochemical properties, and carcinogenic potential of erionite near San Miguel de Allende, Mexico. Environmental Geochemistry and Health 36, 517-529. doi: 10.1007/s10653-013-9578-z.

Pacella A. and Ballirano P., 2016. Chemical and structural characterization of fibrous richterite with high environmental and health relevance from Libby, Montana (USA). Periodico di Mineralogia 85, 169-177. doi: 10.2451/2016PM638.

Pacella A., Ballirano P., Cametti, G., 2016. Quantitative chemical analysis of erionite fibres using a micro-analytical SEM-EDX method. European Journal of Mineralogy 28, 257-264. doi: 10.1127/ejm/2016/0028-2497.

Pacella A., Fantauzzi M., Atzei D., Cremisini C., Nardi E., Montereali M.R., Rossi A., Ballirano P., 2017a. Iron within the erionite cavity and its potential role in inducing its toxicity: Evidences of Fe (III) segregation as extra-framework cation. Microporous Mesoporous Materials 237, 168-179.

Pacella A., Cremisini C., Nardi E., Montereali M.R., Pettiti I., Ballirano P., 2017b. The mechanism of iron binding processes in erionite fibres. Scientific Reports 7, 1319.

Pacella A., Cremisini C., Nardi E., Montereali M.R., Pettiti I., Giordani M., Mattioli M., Ballirano P., 2018. Different erionite species bind iron into the structure: a potential explanation for fibrous erionite toxicity. Minerals 8, 36. doi: 10.3390/min8020036.

Pacella A., Ballirano P., Fantauzzi M., Rossi A., Viti C., Arrizza L., Nardi E., Caprioli R., Montereali, M.R., 2021. Surface and bulk modifications of fibrous erionite in mimicked Gamble's solution at acidic pH. Minerals 11, 914.

Passaglia E., 1970. The crystal chemistry of chabazites. American Mineralogist 55, 1278-1301.

Passaglia E. and Galli E., 1974. Levyne and erionite from Sardinia, Italy. Contributions to Mineralogy and Petrology 43,

253-59. doi: 10.1007/BF00373482.

Passaglia E. and Tagliavini A., 1995. Erionite from Faedo, Colli Euganei, Italy. Neues Jahrbuch Mineralogie-Monatshefte 4, 185-91.

Passaglia E., Artioli G., Gualtieri A., 1998. Crystal chemistry of the zeolites erionite and offretite. American Mineralogist 83, 577-89. doi: 10.2138/am-1998-5-618.

Patel J.P. and Brook M.S., 2021. Erionite asbestiform fibres and health risk in Aotearoa/New Zealand: 1092 A research note. New Zealand Geographer 77, 123-129. doi: 10.1111/nzg.12291

Patel J.P., Brook M.S., Kah M., Hamilton, A., 2023. Global geological occurrence and character of the carcinogenic zeolite mineral, erionite: A review. Frontiers in Chemistry 10, 2022. doi: 10.3389/fchem.2022.1066565.

Peccerillo A., 2005. The Italian Magmatism. Springer-Verlag, Berlin-Heidelberg, 303 pp.

Perini G., Francalanci L., Davidson J.P., Conticelli S., 2004. Evolution and genesis of magmas from Vico Volcano, Central Italy: multiple differentiation pathways and variable parental magmas. Journal of Petrology 45, 139-182-

Petriglieri J.R., Laporte-Magoni C., Salvioli-Mariani E., Ferrando S., Tomatis M., Fubini B., Turci F., 2021. Morphological and chemical properties of fibrous antigorite from lateritic deposit of New Caledonia in view of hazard assessment. Science of the Total Environment 777, 146185. doi: 10.1016/j.scitotenv.2021.146185.

Pollastri S., Gualtieri A.F., Gualtieri M.L., Hanuskova M., Cavallo A., Gaudino G., 2014. The zeta potential of mineral fibres. Journal of Hazardous Materials 276, 469-479. doi: 10.1016/j.jhazmat.2014.05.060.

Pongiluppi D., Passaglia E., Galli E., 1974. Su alcune zeoliti della Sardegna. Società Italiana di Mineralogia e Petrologia 30, 77-100.

Quiroz-Estrada K., Pacella A., Ballirano P., Hernández-Espinosa M. Á., Felipe C., Esparza-Schulz M., 2020. Crystal chemical and structural characterization of natural and cation-exchanged mexican erionite. Minerals 10, 772.

Reed S.J.B., 1993. Electron Microprobe Analysis, second ed. Cambridge University Press, Cambridge, UK.

Rinaudo C. and Croce A., 2019. Micro-Raman spectroscopy, a powerful technique allowing sure identification and complete characterization of asbestiform minerals. Applied Science 9, 3092. doi: 10.3390/app9153092.

Roessner F., Steinberg K.-H., Rechenburg S., 1987. Infrared spectroscopic study of the location of the hydroxyl groups in erionite. Zeolites 7, 488-489.

Rogers A.J., 2018. Exposures estimates of the Wittenoom mining workforce and town residents–implications associated with risk estimation for persons exposed to asbestiform riebeckite. Toxicology and Applied Pharmacology 361, 168-170. doi: 10.1016/j.taap.2018.06.032.

Sabine T.M., Hunter B.A., Sabine W.R., Ball C.J., 1998. Analytical expressions for the transmission factor and peak shift in absorbing cylindrical specimens. Journal of Applied Crystallography 31, 47-51. doi: 10.1107/S0021889897006961.

Saini-Eidukat B. and Triplet J.W., 2014. Erionite and offretite from the Killdeer mountains, Dunn county, North Dakota, USA. American Mineralogist 99, 8-15. doi: 10.2138/am.2014.4567.

Schlenker J.L., Pluth J.J., Smith J.V., 1997. Dehydrated natural erionite with stacking faults of the offretite type. Acta Crystallographica B33, 3265-3268.

Staples L.W. and Gard J.A., 1959. The fibrous zeolite erionite: its occurrence, unit cell, and structure. Mineralogical Magazine 322, 261-281. doi: 10.1180/minmag.1959.032.247.01.

Stephens P.W., 1999. Phenomenological model of anisotropic peak broadening in powder diffraction. Journal of Applied Crystallography 32(2), 281-289. doi: 10.1107/S0021889898006001.

Sullivan P.A., 2007. Vermiculite, respiratory disease, and asbestos exposure in libby, Montana: update of a cohort mortality study. Environmental Health Perspectives 114, 579-585. doi: 10.1289/ehp.9481.

Sweatman T.R. and Long J.V.P., 1969. Quantitative electron-probe microanalysis of rock-forming minerals. Journal of Petrology 10, 332-379. doi: 10.1093/petrology/10.2.332.

Turci F., Tomatis M., Compagnoni R., Fubini B., 2009. Role of associated mineral fibres in chrysotile asbestos health effects: the case of balangeroite. The Annals of Occupational Hygiene 53, 491-497. doi: 10.1093/annhyg/mep028.

Young R.A., 1993. Introduction to the Rietveld method. In The Rietveld Method; Young, R.A., Ed.; Oxford University Press: Oxford, UK, 1-38.

Zoboli A., Di Giuseppe D., Baraldi C., Gamberini M.C., Malferrari D., Urso G., Lassinantti Gualtieri M., Bailey M., Gualtieri A.F., 2019. Characterisation of fibrous ferrierite in the rhyolitic tuffs at Lovelock, Nevada, USA. Mineralogical Magazine 83, 577-586.